Controlled mechanical failure in glasses via designed spatial inhomogeneity

Vinay Vaibhav,[1,2,3,*] Jürgen Horbach,[4,†] and Pinaki Chaudhuri[1,2,‡]
[1]*The Institute of Mathematical Sciences, CIT Campus, Taramani, Chennai 600113, India*
[2]*Homi Bhabha National Institute, Anushaktinagar, Mumbai 400094, India*
[3]*Department of Physics "A. Pontremoli", University of Milan, Via Celoria 16, 20133 Milan, Italy*
[4]*Institut für Theoretische Physik II, Heinrich-Heine-Universität Düsseldorf, Universitätsstraße 1, 40225 Düsseldorf, Germany*

(Received 23 April 2023; revised 2 July 2023; accepted 18 July 2023; published 11 September 2023)

In glasses under mechanical load, intrinsic spatial inhomogeneities at specific locations in the sample may cause shear banding. This allows us to initiate mechanical failure in a controlled manner. We perform molecular dynamics simulations to investigate inhomogeneous glass states under shear, using two different protocols to obtain these spatial inhomogeneities, viz., (i) by applying a temperature pulse, and (ii) by generating regions with a different degree of annealing via the swap Monte Carlo technique. In both cases, we find that shear banding is associated with a subtle interplay between stochasticity and local potential energy.

DOI: 10.1103/PhysRevMaterials.7.095601

I. INTRODUCTION

A focus of the recent simulation studies on structural glasses under mechanical load (e.g., an external shear) has been on the question of which conditions lead to a ductile or brittle response of these systems [1–11]. One of the central results of these studies is the finding that the nature of this response, i.e., whether it is ductile or brittle, depends on the degree of annealing of the initial glass sample that is put under mechanical load. As a matter of fact, a larger degree of annealing leads to a more brittle response. In the framework of the athermal quasistatic shear protocol, it has been conjectured that there is a ductile-to-brittle transition, controlled by the degree of annealing of the initial glass sample, that falls in the universality class of the random-field Ising model [5]. A view that is different from this zero-temperature picture has been recently put forward [11] based on simulations of deeply supercooled and fully equilibrated liquids under shear far below the critical temperature, T_c, of mode-coupling theory (MCT) [12]. Here, it has been shown that for temperatures $T < T_c$, there is a finite timescale $\tau_{\rm lt}$ over which the supercooled liquid can be considered as an amorphous solid. This timescale rapidly increases with decreasing temperature. As a consequence, at sufficiently low temperatures $T < T_c$, there is a window of shear rates $\dot{\gamma}$ with $\dot{\gamma}^{-1} < \tau_{\rm lt}$ where the response of the supercooled liquid to the external shear is brittle. Here, the brittle response is reflected by a sharp stress drop in the stress-strain relation (sharp refers to a drop on a strain scale much smaller than 0.1) and the nucleation of a shear band, i.e., the occurrence of a bandlike structure with a much higher mobility than in the rest of the system.

In the latter case, shear banding happens as the response of a fully equilibrated, deeply supercooled liquid to the external shear at a constant shear rate. As mentioned above, such a system can be in an amorphous solid state over a finite but very long timescale. The situation is more complicated when one considers the shear response of a glass sample, i.e., a system which is in a nonequilibrium state. In such systems, shear banding is a ubiquitous phenomenon [1,13–34] and there can be interference with aging processes and inhomogeneities due to the fast quench from a high temperature to the target temperature of the glass sample. These features can be associated with soft regions in the system that can initiate the nucleation of a shear band. It has been demonstrated in a computer simulation by Ozawa *et al.* [35] how microscopic failure starts from a synthetic soft region with the nucleation of a shear band. In a simulation study by Varnik *et al.* [21], it has been shown that shear bands can be initiated at the walls by which the glass sample is confined. For homogeneous glass samples with periodic boundary conditions, there are different views on the question of whether structural inhomogeneities in the initial undeformed glass sample determine the location of a shear band [36] or whether the formation of a shear band is linked to stochasticity and the details of the shear protocol [31,33].

In experimental glass samples or in glass materials during the production process, there is often some manufacturing glitch that causes nucleation of shear bands at specific locations. For this kind of heterogeneous nucleation process, there is no clear picture of how the shear band forms, under ambient thermal conditions, from whatever soft spot caused by inhomogeneities due to the production protocol of the glass sample. In this work, we are aiming at a better understanding of this issue using nonequilibrium molecular dynamics computer simulations of model glass formers. The central idea of our approach is to implement in a controlled manner inhomogeneities in glass samples and identify the local soft spots that are responsible for the heterogeneous nucleation of a shear band. With regard to the key features to design materials with a predetermined failure pathway, this approach is also interesting for applications.

*vinay.vaibhav@unimi.it
†horbach@thphy.uni-duesseldorf.de
‡pinakic@imsc.res.in

To demonstrate the generality of our findings, we present our observations for two different protocols of preparing inhomogeneous glass samples, for which we use different model glass formers: (i) In the first protocol, the inhomogeneity is caused by a temperature gradient, as often present in typical production processes of metallic glasses. We consider a Kob-Andersen binary Lennard-Jones mixture [37]. As in an earlier study [38], we start with a spatially homogeneous glass state and then introduce a pulse of temperature gradient. The temperature gradient causes a spatial inhomogeneity of density and concentration. After removing the gradient, due to the very slow structural relaxation process in the glass state, the inhomogeneity created by the thermal gradient does not completely vanish and one obtains samples with a spatially dependent density profile. (ii) In the second protocol, inhomogeneities are incorporated via different levels of local annealing in the sample such that a fully equilibrated ultrastable state coexists with a poorly annealed glass state. A polydisperse soft-sphere mixture is considered that has been introduced by Ninarello *et al.* [39], using a version of this model that has been introduced in Ref. [40] (see below). This model allows the efficient application of the swap Monte Carlo (SMC) technique [11,39,41,42], from which one may obtain fully equilibrated samples at very low temperature, i.e., far below the critical temperature of MCT. Now, the idea is to apply the SMC only to a spatially restricted part of the system. As a result, one obtains inhomogeneous samples where a poorly annealed region coexists with a fully equilibrated region (the two regions are separated by interfaces). Then, the samples, as described in (i) and (ii), are sheared and we investigate the mechanisms of shear band nucleation at the yielding transition.

II. PROTOCOLS, MODELS, AND METHODS

In this section, we describe the two protocols that we have used to prepare inhomogeneous glassy states whose mechanical response we probe, motivated by possible practical scenarios. In the first case, we consider inhomogeneous thermal conditions encountered during generic glass manufacturing or due to nonuniform heating (e.g., see Refs. [43–48]), and therefore we study states prepared by exposing homogeneous glassy samples to a thermal gradient pulse. In the second case, we consider the situation where the local annealing can be spatially controlled which would lead to glassy states having different local stability, taking advantage of recent progress in numerical annealing techniques to access glasses with higher stability, as discussed above. As is evident, our choice of protocols is motivated from practical physical experiences, but are just two examples of a myriad of scenarios which can lead to marked spatial heterogeneities within a glass.

A. Preparing the spatially inhomogeneous glassy states

1. Protocol 1: Preparing inhomogeneous states applying temperature gradient pulse

For the first protocol (referred to here as *protocol 1*), we consider the Kob-Andersen 80-20 (AB) binary Lennard-Jones mixture [37], using the same version of this model as in previous works [32,33]. The range of the interactions is set to $R^c = 2.5\sigma_{\alpha\beta}$ with $\{\alpha, \beta\} \in \{\mathrm{A}, \mathrm{B}\}$. We work at a number density of 1.2 and consider systems with $N = 48\,000$ particles in a three-dimensional rectangular box with linear dimensions $L_x = L_y = 20$ and $L_z = 100$, applying periodic boundary conditions in all three directions. We perform our molecular dynamics (MD) simulation using LAMMPS [49]. The equations of motion are integrated via the velocity form of the Verlet algorithm with time step $\Delta t = 0.005$. All measured quantities are given in Lennard-Jones units, where lengths and energies are expressed in units of σ_{AA} and $\varepsilon_{\mathrm{AA}}$, respectively. The unit of time is $\sqrt{m\sigma_{\mathrm{AA}}^2/\varepsilon_{\mathrm{AA}}}$.

A schematic of the protocol for preparing the inhomogeneous glassy states is provided in Figs. 1(a)–1(c). We first equilibrate the system in a supercooled liquid state at $T = 0.45$. The equilibrated independent configurations are quenched to $T_C = 0.2$ (i.e., below $T_{\mathrm{MCT}} \approx 0.435$) and subsequently aged for $t_{\mathrm{age}} = 10^4$; see Fig. 1(a), labeled as step 1. Then, a temperature gradient pulse is applied along the

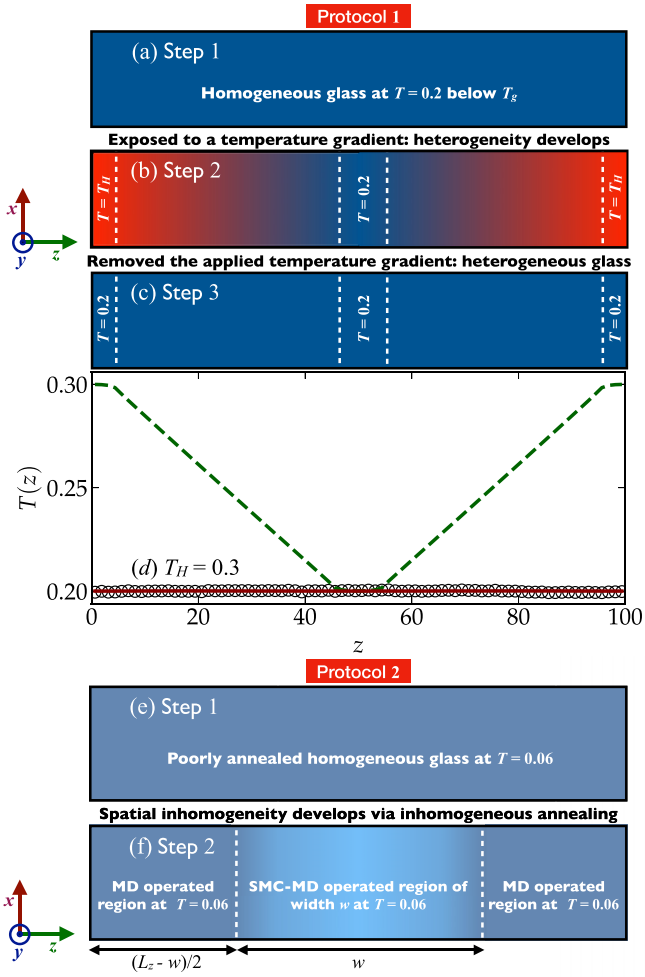

FIG. 1. Preparation of spatially inhomogeneous glassy states, with z axis being the direction of spatial variation. [(a)–(c)] Schematic for protocol 1; (d) corresponds to the temperature profiles $T(z)$ obtained during step 1 in (a) (solid red line), step 2 in (b) for $T_H = 0.3$ (dashed green line), and step 3 in (c) (open black symbols). [(e),(f)] Schematic for protocol 2. See text for details of the steps.

z direction [38]: extreme ends with width $L_z/20$ each (hot zone) maintained at temperature T_H and a central region with width $L_z/10$ (cold zone) is maintained at T_C; see Fig. 1(b), labeled as step 2. This local thermostatting is done using a Langevin thermostat with a dissipation timescale of $\tau_d = 0.5$. The samples are exposed to a thermal gradient pulse for the exposure time $t_{\rm exp}$ such that the temperature of the cold zone is maintained at $T_C = 0.2$ and that of the hot zone at $T_H = 0.3, 0.4, 0.5$; the resultant temperature profile $T(z)$ is shown in Fig. 1(d). In a next step, the gradient is switched off by having both the zones at the same temperature $T_H = T_C = 0.2$, for a period of 5×10^4; see Fig. 1(c), labeled as step 3. These states are then subjected to external shear to probe their mechanical response. We consider 24 initial states, prepared via independent N-particle MD trajectories, to construct the ensemble for our study.

2. Protocol 2: Preparing inhomogeneous states via spatially inhomogeneous annealing

In the second protocol (labeled *protocol 2*), we use a polydisperse soft-sphere model, introduced by Ninarello *et al.* [39] and subsequently investigated in different contexts; e.g., see Refs. [5,11,40,50]. The diameters of the particles are chosen according to model $\mathcal{D}$ in Ref. [40]. The range of interaction between two particles i and j has a cutoff (based on their interparticle separation) $R^c_{ij} = 1.25\sigma_{ij}$, where σ_{ij} is calculated using the diameters σ_i and σ_j of the particles. The details of the model potential can be found in Refs. [11,39,40].

We work at a number density of 1.0 and again we consider a rectangular geometry of the simulation box, with linear dimensions $L_x = L_y = 12$ and $L_z = 80$, considering systems with $N = 11\,520$ particles. A schematic of the protocol for preparing the inhomogeneous glassy states is provided in Figs. 1(e)–1(f). At first, we equilibrate the system at temperature $T = 0.15$, which is above the critical mode-coupling temperature $T_{\rm MCT} = 0.104$. We use the hybrid swap Monte Carlo–molecular dynamics (SMC-MD) algorithm, as discussed in [11]. This corresponds to attempting N particle diameter swaps every 25 MD steps, which are accepted or rejected based on a Metropolis criterion. During the MD simulation, the equations of motion are integrated using the velocity form of the Verlet algorithm with time step $\Delta t = 0.01$.

We prepare three different types of states at $T = 0.06$, which we refer to in the following as poorly annealed (PA) states, well-annealed (WA) states, and inhomogeneously annealed states. The PA states are prepared by quenching the system from $T = 0.15$ to $T = 0.06$ and then we age them for $t_{\rm age} = 2 \times 10^5$, coupling the MD simulation (using $\Delta t = 0.01$) to a Berendsen thermostat, labeled as step 1 in Fig. 1(e). The inhomogeneously annealed states are thereafter prepared, using the PA states, by applying the SMC-MD algorithm to a small region $L_x \times L_y \times w$, i.e., having width w along the z direction at the middle of the simulation box, while the dynamics in the other region of the simulation box proceeds via usual molecular dynamics, labeled as step 2 in Fig. 1(f). This allows faster annealing in the central region, compared to the region where only MD is utilized. This inhomogeneous annealing protocol is continued for 2×10^5. The WA states are prepared by quenching high-temperature states at $T = 0.15$ to $T = 0.06$, followed by equilibration using SMC-MD, thereby generating fully equilibrated states at this temperature. In each case, we prepare 32 independent samples, which are then used for studying the response to imposed shear.

B. Studying response to shear deformation

After preparing the different samples, using the two protocols mentioned above, we study the shear response by deforming the xz plane along the x direction with different rates $\dot\gamma$, using Lees-Edwards boundary conditions. When the shear process is on, the temperature is controlled using a dissipative particle dynamics (DPD) thermostat [51].

Apart from monitoring the macroscopic shear stress and energy that develops due to the imposed shear, we also probe some of these observables at the local scale in the form of spatial profiles along the z direction, i.e., along the shear gradient direction, in order to provide spatial information regarding the response to applied shear. We also study the resultant microscopic dynamics, specifically the local nonaffine displacements. For that purpose, we construct three-dimensional maps of local mobility, which have been used in earlier studies [33] to demonstrate the emergence and evolution of the flow heterogeneities in the form of shear bands. To construct these maps at different macroscopic strain values, we use the single-particle squared displacement along z, i.e., in the direction transverse to the applied shear, measured with respect to the quiescent undeformed state prior to application of shear at $t = 0$, to characterize the mobility of the particle. In the rendering of the map, each particle is colored with the magnitude of its mobility, with the coordinates of the particles corresponding to locations at the strain at which the map is being constructed; for ease of visual depiction, we display a two-dimensional cut of the three-dimensional map along the xz plane at $y = 0$.

III. RESULTS

A. Characterizing inhomogeneous glassy states

We first characterize, in the quiescent state, the spatially inhomogeneous glassy states generated via the two protocols outlined above. As noted above, the z axis is the direction along which the spatial heterogeneity is developed using the protocols discussed. The subsequent shear is applied along the xz plane; i.e., the shear gradient is along the direction of spatial heterogeneities imprinted prior to shear.

1. Protocol 1

First, we discuss changes of the spatial properties of the glassy samples as a consequence of the exposure to the pulse of the thermal gradient. For convenience, we define normalized local density as $\tilde\rho(z) \equiv \rho(z)/\bar\rho$, where $\rho(z)$ is the local number density and the global parameter $\bar\rho = 1.2$ is the average number density. The aged glassy sample, in the absence of the thermal protocol discussed above, is expected to have no spatial variation of $\tilde\rho(z)$ and local potential energy $U(z)$, barring some sample-to-sample noisy fluctuations, as shown with

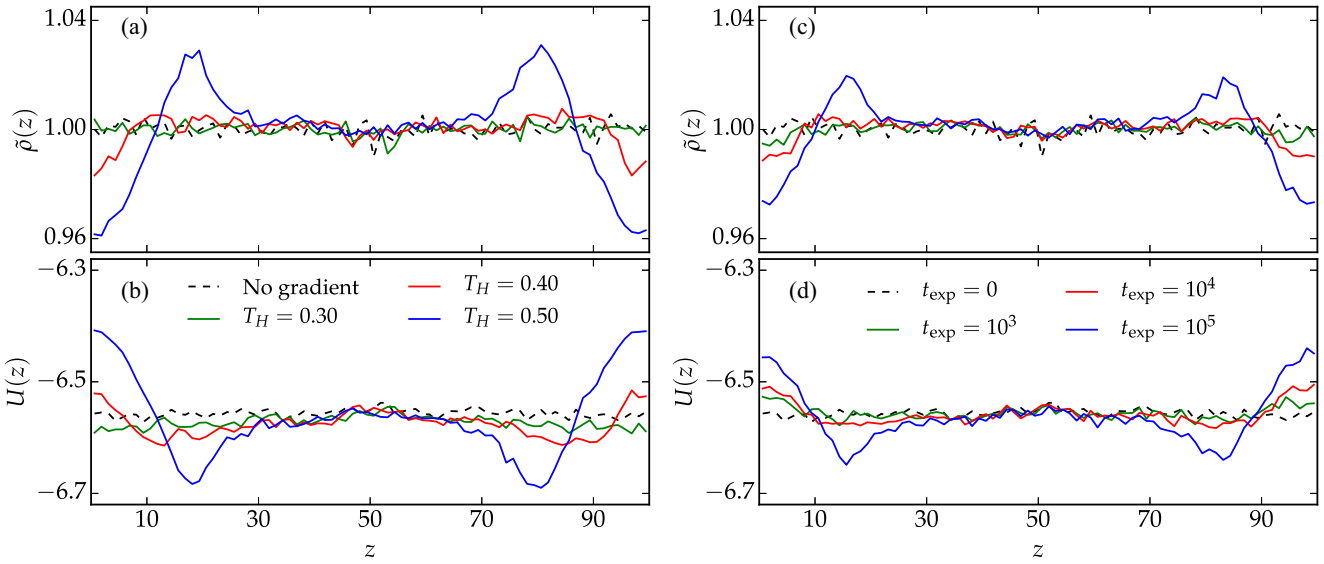

FIG. 2. Response to thermal gradient pulse. Measurement of spatial profiles of normalized density $\tilde{\rho}(z)$ and potential energy $U(z)$ along the z direction, averaged over a period of 5×10^4 after the imposed thermal gradient is switched off. [(a),(b)] Spatial profiles are shown for different temperature gradients ($T_C = 0.20$ and $T_H = 0.30$, 0.40, 0.50) but with fixed exposure time, i.e., $t_{\rm exp} = 5 \times 10^5$, including the case which has not been exposed to the temperature gradient. [(c),(d)] Spatial profiles are shown for samples processed through a fixed temperature gradient ($T_C = 0.20$ and $T_H = 0.50$) but exposure time of $t_{\rm exp} = 0$, 10^3, 10^4, 10^5. Profiles have been computed via a spatial discretization of $\delta z = 1.25$.

the dotted black line in Fig. 2. Note that the spatial profiles along the z direction are computed by averaging along the x and y directions, using a spatial discretization in z. Also note that for building the energy profiles $U(z)$, a time-averaging is done to smooth out fluctuations from thermal vibrations; since these measurements are done in the glassy state over small time windows, it has the necessary information about the mean local structure.

When the thermal gradient is switched on, the region where the local temperature is high will start relaxing (and even melting for $T > T_{\rm MCT}$) with relatively higher mobility, leading to local structural changes; this is a manifestation of the Soret effect in glassy systems as reported earlier [38]. These changes will keep evolving while the gradient is on. But as soon as the gradient is switched off and the sample is back to a glassy environment at T_c, the evolving structural changes almost freeze which leads to an inhomogeneous glassy sample with spatial variation of $\tilde{\rho}(z)$ and $U(z)$ [38]; i.e., the glassy sample retains the history of the local thermal environment it had been subjected to via the gradient pulse. The spatial measurements over a time span of 5×10^4 after switching off the gradient are shown in Fig. 2. Note that we have checked and found that the aging process of these profiles is extremely slow. This is expected because after the thermal gradient is switched off, the whole sample instantaneously returns back to a glassy environment at temperature $T_C = 0.2$, where any structural rearrangements hardly occur on the viable timescale of the simulation.

In Figs. 2(a) and 2(b), measurements are shown after applying the different thermal gradients ($T_C = 0.2$ and $T_H = 0.3$, 0.4, 0.5) for $t_{\rm exp} = 5 \times 10^5$, and then switching them off. It is evident that the spatial variation in the profiles becomes more prominent if the gradient is bigger. If we look at the normalized density [Fig. 2(a)], we find that the local relaxation or melting near the hotter ends causes local expansion of the material, when the gradient is switched on, leading to local decrease in density which is retained when the thermal gradient is switched off. Due to this local expansion, this leads to the regions close to hotter regions being pushed inward. In the middle of the material, the density is roughly not affected, since this region is always at $T_C = 0.2$. Therefore, in the intermediate region, there is a compression effect leading to an increased local density, as is visible. As reported earlier [38], this spatial variation in density is caused via the mobility of the smaller species when the thermal gradient is switched on. The spatial reorganization also affects the local potential energy; see Fig. 2(b). However, there is a peculiar feature which will become significant when we discuss the shear response. In all cases, when the thermal gradient is switched on, the hotter end has higher potential energy. When the gradient is switched off, for $T_H = 0.4$, 0.5, the erstwhile hot zones still continue to have higher potential energy and the immediate neighboring region has relatively lower potential energy because of the density compression, as discussed above. But for the case of $T_H = 0.3$, we observe that the thermal fluctuations lead to better local annealing at the erstwhile hot ends and thereby lower potential after the gradient is switched off. Below, we will further discuss the consequences of these spatial inhomogeneities that develop via this protocol of thermal pulsing.

In Figs. 2(c) and 2(d), we show the spatial variation of the quantities measured after applying the thermal gradient by having $T_C = 0.2$ and $T_H = 0.5$ for a period of $t_{\rm exp} = 10^3$, 10^4, 10^5. Again, these spatial measurements are done over a period of 5×10^4 after switching off the gradient. It is very clear that the heterogeneity in terms of local density and local potential energy increases with the increase in the exposure time of the gradient. Longer exposure keeps the melting/relaxation

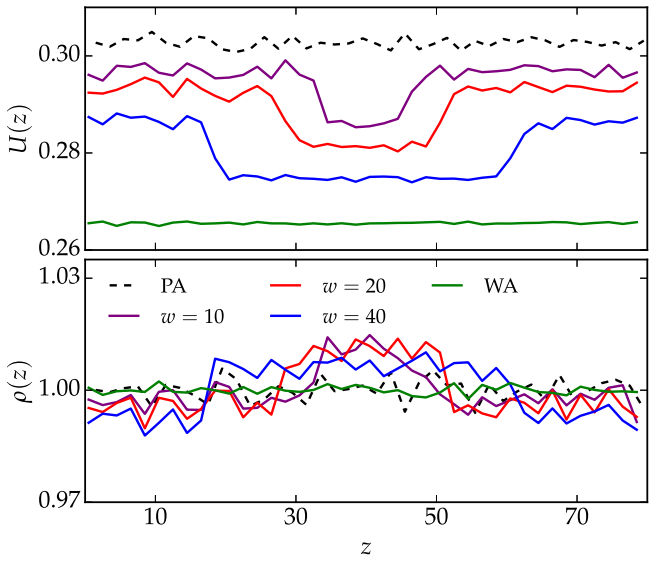

FIG. 3. Response to spatial annealing. Ensemble-averaged spatial profiles of potential energy, $U(z)$ (top), and density $\rho(z)$ (bottom) for homogeneously and inhomogeneously swap-annealed glassy states, as labeled. The case of the poorly annealed states is also shown for comparison. The profiles are obtained via time-averaging over a period of $t = 10^4$, and by using a spatial discretization of $\delta z = 2.0$.

process on near the hotter end, resulting in the increase of the heterogeneity.

2. Protocol 2

We do a similar characterization of the potential energy and density profiles that are observed via the other protocol, viz., regions within the sample (having varying widths) being annealed at different rates. In Fig. 3, we plot the spatial profiles $U(z)$ and $\rho(z)$ for different widths w of the annealing region. We compare the observed profiles with those for the PA and WA samples. In $U(z)$, we observe that in the region where the swap annealing is done along with the MD, the local energy is lower: the larger this annealing region, the lower the energy. However, this lower local energy does not reach the energy level achieved when the full system is annealed using SMC. Note, there is also a variation in local density; there is an increase in the region where the swap annealing is done, i.e., where the energy is lower, and therefore a decrease in the region where SMC is not applied, since the overall density is constant. This is unlike the cases of PA or WA states where the density is spatially uniform; the presence of the interface in the case of inhomogeneous annealing allows for local volume fluctuations. Due to this decrease in density in the region outside of where SMC is applied, we also note a variation in the local energy; lowering of the local density leads to lower local energy.

To summarize this discussion, we have been able to prepare glassy samples with controlled spatial heterogeneity in energy or density. For the case of the applied thermal gradient, we call those states *thermally processed samples*, and in the case of the other protocol, we label those as *spatially annealed states*.

B. Macroscopic shear response

As described above, we obtain glassy samples with spatial inhomogeneity in the z direction. These samples are sheared in the x direction by deforming the xz plane with fixed shear rate $\dot{\gamma}$ so that the density heterogeneity in the z direction is part of flow gradient direction. Our goal is to compare the shear response of the spatially inhomogeneous glassy samples with that of the spatially homogeneous samples, corresponding to the two models and protocols discussed above. The mechanical response is quantified by measuring the stress-strain behavior and the evolution of average potential energy $\langle U \rangle$ of the system with strain, which we discuss in detail below.

The shear stress σ_{xz} is calculated using the Irving-Kirkwood expression: $\sigma_{xz} = \langle \sum_{\alpha\beta} f^x_{\alpha\beta} r^z \rangle / V$, where $f^x_{\alpha\beta}$ is the x component of the force acting between a pair of particles (labeled α and β, which could belong to either species) and r^z is the z component of the distance vector between these two particles. V is the total volume of the simulated system. $\langle \cdot \rangle$ corresponds to averaging over independent samples.

A typical glassy system under shear responds elastically with the linear increase in stress for small deformation followed by a stress overshoot, which then relaxes and reaches a steady state. Similarly, the average potential energy increases, due to the increasing deformation under applied shear, and goes to a steady value at long times. Below, we discuss how the structural heterogeneities imprinted into the initial states via the two protocols influence the macroscopic response.

1. Protocol 1

In Fig. 4, we show the shear response of the thermally processed states; the results correspond to an applied shear rate of 10^{-3}. In Figs. 4(a) and 4(b), we show the data for varying thermal gradient and in Figs. 4(c) and 4(d), for a fixed thermal gradient but varying the exposure time $t_{\rm exp}$.

If we look at the data of the ensemble-averaged shear stress (σ_{xz}) as a function of strain (γ), the initial increase of stress is almost similar for both processed and unprocessed samples, hinting that the modulus of the material is not much affected; see Fig. 4(a). But with the increase in strain, the behavior of the thermally processed states starts to show differences. If we consider the states which had $T_H = 0.5$ during the duration of the thermal gradient pulse, the height in the stress overshoot is not only lower compared to the unprocessed states but also occurs at a smaller strain and then relaxes faster; see inset of Fig. 4(a). On the other hand, for smaller applied gradients, where $T_H = 0.3$, 0.4, the stress overshoot has higher values than for the unprocessed samples [see inset of Fig. 4(a)], implying that their response is more rigid. When the exposure time ($t_{\rm exp}$) is varied keeping the thermal gradient fixed ($T_H = 0.5$), we observe that with the increase in exposure time, the height of the stress overshoot progressively decreases and the stress relaxation happens earlier [see Fig. 4(c) and the corresponding inset]; i.e., we obtain an increasingly softer response with increasing $t_{\rm exp}$. Hence, these observations indicate that the thermal processing modifies the yielding response of the glassy state, due to the spatial inhomogeneities that have been developed via the gradient pulsing.

The evolution of the ensemble-averaged potential energy $\langle U \rangle$ with strain is shown in Figs. 4(b) and 4(d). We observe

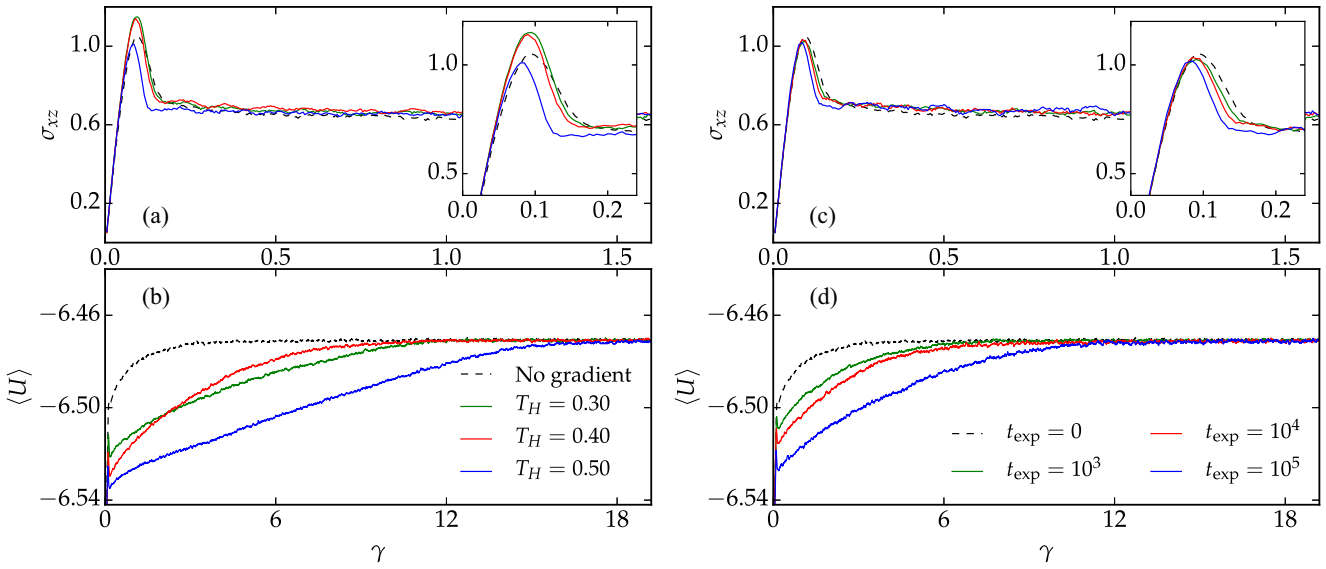

FIG. 4. Shear response of thermally processed inhomogeneous glassy states. Shear stress σ_{xz} and potential energy $\langle U \rangle$ are shown when the system is sheared with shear rate $\dot{\gamma} = 10^{-3}$. [(a),(b)] Measurements are shown for samples processed through different temperature gradients ($T_C = 0.20$ and $T_H = 0.30$, 0.40, 0.50) but with fixed exposure time $t_{\rm exp} = 5 \times 10^5$, including the case which has not been exposed to the temperature gradient. [(c),(d)] Measurements are shown for samples processed through a fixed temperature gradient ($T_C = 0.20$ and $T_H = 0.50$) but exposure time of $t_{\rm exp} = 0$, 10^3, 10^4, 10^5. Insets in [(a)–(c)] show a zoom into the stress evolution, for all cases, around the yielding regime.

that in both situations, the steady state for thermally processed samples is achieved at relatively large values of strain, compared to the unprocessed state. For example, for the case of $T_H = 0.5$, it seems to be around 15 times the value of the strain at which the steady state is achieved for unprocessed samples. Also, as the thermal gradient or exposure time is increased, the timescale to reach the steady state is observed to increase. This means that the timescale for obtaining the steady state is linked to the extent of structural heterogeneity along the shear-gradient plane. This increase in timescale to attain steady state with the increase in inhomogeneity is expected. Shear will try to homogenize the material and that would be the steadily flowing state. This happens relatively quickly in the unprocessed sample. However, as we see, the homogenization process slows down with the increase in spatial inhomogeneity in the initial glassy state. This prolonged homogenization process also suggests spatial inhomogeneities in the dynamics, which we analyze below.

2. Protocol 2

We do a similar analysis for the states generated via spatially dependent annealing; see Fig. 5 for the data showing the response to an imposed shear rate of $\dot{\gamma} = 10^{-4}$. In the case of shear stress [Fig. 5(a)], the response is most dramatic for the WA state, where a large stress overshoot followed by a sudden brittle-like stress drop is observed, consistent with previous studies [11]. For the locally annealed states, the height of the stress overshoot is more similar to the case of the PA state. However, the stress relaxation happens quicker for the more locally annealed states; see inset of Fig. 5(a). The evolution of energy [Fig. 5(b)] follows a systematic pattern: the PA state reaches steady state quickly, the WA state has the slowest approach to steady state, and the locally annealed states have trends in between. It is therefore pertinent to note that the attainment of steady state depends upon the degree of annealing, and not spatial heterogeneity *per se*; the more annealed states are far from reaching the steady state within the time window of our observation (which is fairly large).

To summarize, we observe changes in the macroscopic response, be it in the height of the stress overshoot or the subsequent stress relaxation or the eventual reaching of steady

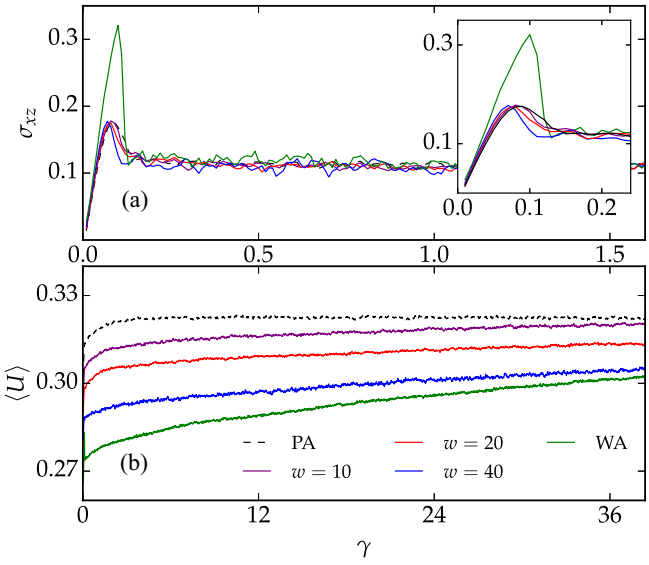

FIG. 5. Shear response of spatially annealed glassy states. Evolution of ensemble-averaged (a) shear stress σ_{xz} and (b) potential energy $\langle U \rangle$ with strain γ, in response to imposed shear rate of $\dot{\gamma} = 10^{-4}$, for different scales of spatial annealing, as labeled. The response of the PA states is also shown for comparison. Inset in (a) shows a zoom into the stress evolution, for all cases, around the yielding regime.

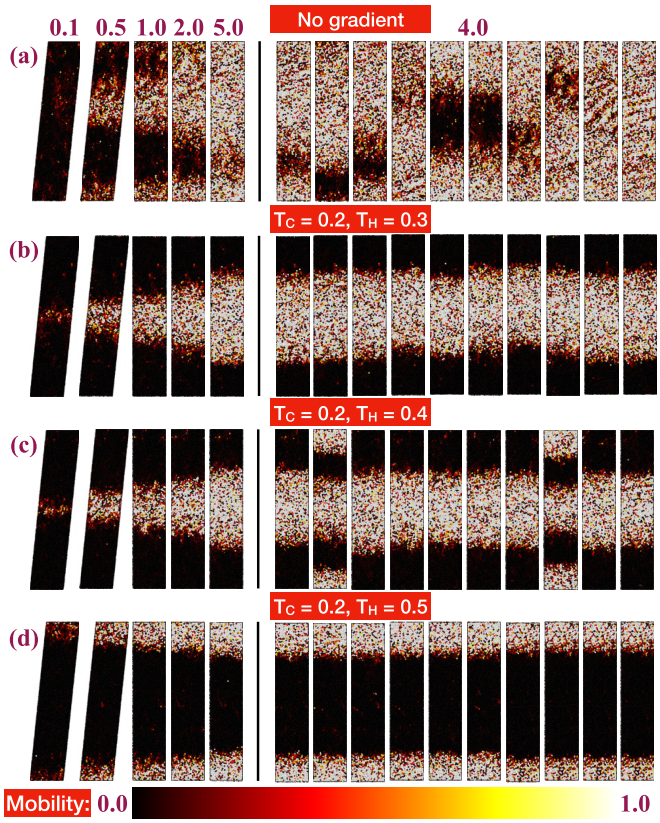

FIG. 6. Mobility maps of sheared thermally processed samples: impact of gradient. A pulse of thermal gradient, with $T_C = 0.20$ and $T_H = 0.30$, 0.40, 0.50 (as marked), are applied for $t_{\text{exp}} = 2 \times 10^5$ to generate inhomogeneous glassy samples and then these samples are sheared with shear rate $\dot{\gamma} = 10^{-4}$. Maps on the left side of the vertical line show the evolution of shear bands with strain $\gamma = 0.1$, 0.5, 1.0, 2.0, 5.0 (also marked), while maps on the right side are shown at the fixed value of strain $\gamma = 4.0$ and starting with the same thermally processed sample but different random seed for DPD thermostat. In the upper panel, labeled (a), maps are shown for the case of unprocessed samples.

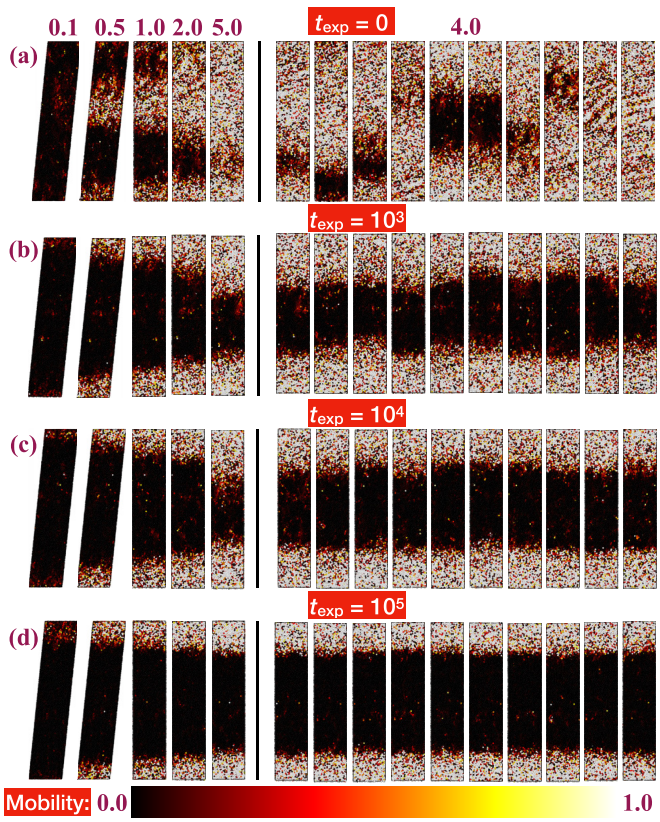

FIG. 7. Mobility maps of sheared thermally processed samples: impact of exposure time. A fixed temperature gradient pulse with $T_C = 0.20$ and $T_H = 0.50$ is applied for different duration $t_{\text{exp}} = 0, 10^3, 10^4, 10^5$ (also marked) to generate inhomogeneous glassy samples and then these samples are sheared with shear rate $\dot{\gamma} = 10^{-4}$. Maps on the left side of the vertical line show the evolution of shear bands with strain $\gamma = 0.1$, 0.5, 1.0, 2.0, 5.0 (also marked), while maps on the right side are shown at the fixed value of strain $\gamma = 4.0$ and starting with the same thermally processed sample but different random seed for DPD thermostat. In the upper panel, labeled (a), maps are shown for the case of unprocessed samples.

state, due to the presence of spatial heterogeneities imprinted in the quiescent glassy states via the protocols of preparation that we have followed. We now proceed to discuss the spatial manifestations of the response, as detailed in the following subsection.

C. Nucleation and evolution of shear bands

To examine the microscopic dynamical response of these states to the applied shear, for a chosen initial state, we compute the mobility maps using single-particle squared displacement $\delta r_z^2(t)$, measured with respect to the state at $t = 0$, i.e., at the start of shear. These maps have been calculated at different strain values, using an imposed shear rate of 10^{-4}. The flow behavior in terms of such mobility maps has been used in earlier studies [33] to probe the emergence and evolution of the flow heterogeneities in the form of shear bands. We compare the maps for the different initial states that we have generated, viz., those with and without structural heterogeneity.

1. Protocol 1

We first focus on the states generated via the thermal gradient processing. In Fig. 6, we present the mobility maps at the different strain values, for the untreated glassy samples [Fig. 6(a)] and glassy samples treated via different temperature gradients ($T_C = 0.20$ and $T_H = 0.30$, 0.40, 0.50); see Figs. 6(b)–6(d). On the left side of the vertical line in Fig. 6, the maps have been shown at strain values of 0.1, 0.5, 1.0, 2.0, 5.0. In the unprocessed sample, at small strains, we observe a few hot spots at random locations, which then merge to form a shear band and then the mobility gets spatially homogenized at a strain value of 4.0. But inhomogeneous samples show very sharp localized band patterns at early strain. The expansion of these shear bands becomes slower or the lifetime of shear bands becomes longer for the states which had been subjected to bigger gradients; we can observe it visually by comparing the bands at a particular strain value for different thermal processing histories. This observation is consistent with the macroscopic observations made above; viz., with the increase in spatial inhomogeneity in the undeformed state

prior to shear, the sample takes a longer time to reach a steady state. We also note that for $T_H = 0.3$, the shear band (faster region) nucleates in the middle of the sample, i.e., near the region that was the colder end during the thermal pulse, and it expands toward the region that was the hotter region, while for $T_H = 0.5$ the band nucleation happens in the region that was at higher temperature during the thermal pulse. The case for $T_H = 0.4$ is a bit mixed, with the shear band usually forming at the middle of the sample; however, there are cases where shear bands are visible simultaneously at the ends that were either hot or cold. For the different thermal processing histories, the difference in the location of the shear band formation could be due to relative local stability that has its origin in the spatial heterogeneity of the initial state, to be discussed further below.

We note that the rectangular geometry of the sample suppresses some fluctuations which delays the propagation of the mobility across the z direction. However, this effect will be similar in all the cases discussed above. Thus, the delay in propagation that we observe with increasing spatial heterogeneity of the initial state is entirely emerging from the variation in local structure encoded via the thermal processing.

In Figs. 7(a)–7(d), we present the location of the shear bands at the different strain values for the glassy samples treated using a fixed thermal gradient ($T_C = 0.2$ and $T_H = 0.50$) but different exposure time $t_{\text{exp}} = 0$, 10^3, 10^4, 10^5. In this case, the main observation is that the lifetime of the band increases with the increase in the time window over which the initial states were exposed to the thermal gradient. This observation is consistent with the macroscopic measurements in Fig. 4(d), where we observed that the timescale of reaching steady state increases with the increase in exposure time. The location of the shear band is roughly the same in all cases of finite exposure time in Figs. 7(b)–7(d), similar to the case of Fig. 6(d), where the same gradient is applied for $t_{\text{exp}} = 2 \times 10^5$; i.e., a shear band always nucleates near the extreme ends close to the hotter region.

Next, we investigate whether the initial structure in the undeformed state determines the location of the flow bands observed under the imposed shear. For this purpose, we start with an inhomogeneous glassy sample obtained after switching off the gradient and perform at least 10 different shear deformation simulations with $\dot{\gamma} = 10^{-4}$, using different random seeds for the DPD thermostat which maintains the temperature at 0.2. Hence, for each run, the sample is same, with its unique spatial heterogeneities, but the random kicks faced by particles during deformation are different. On the right side of the vertical line in Fig. 6, we show the mobility map at the strain value of $\gamma = 4.0$ for 10 different simulations with the same initial inhomogeneity at the start of deformation. In all samples, except for the case of a few samples at $T_H = 0.4$, mobility maps show similar patterns; i.e., for $T_H = 0.3$, 0.4 a shear band nucleates close to what was the colder region when the thermal gradient was switched on and expands toward what was the hotter region, and for $T_H = 0.5$ the shear band always nucleates near the erstwhile hotter region at extreme ends and then expands toward the colder region. This is in contrast to the unprocessed sample where the slower regions are located at different levels along z, which is consistent with previous observations [33]. Therefore, for the thermally processed samples, we can conclude that there is no run-to-run variation; i.e., there is no stochastic effect in the selection of the location, unlike the case of the unprocessed states [33]. Hence, this selection of the location of shear band formation must be related to features in the initial structure, viz., in the form of structural heterogeneities, which we further elucidate below. A similar exercise is also done for the case of samples having different exposure time; see the right column of Fig. 7. There too, we observe no run-to-run variation, especially for samples which have been exposed to the thermal gradient for long times.

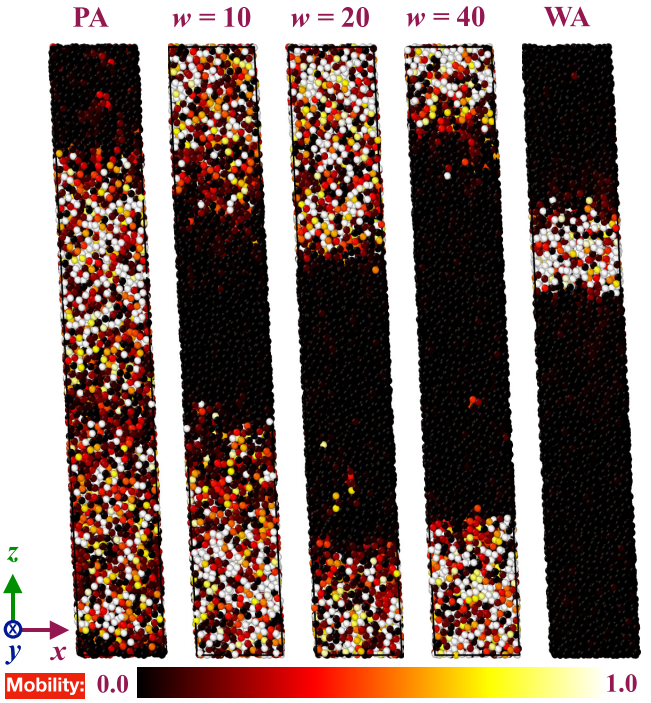

FIG. 8. Mobility maps of sheared spatially annealed samples. Maps showing spatial response under imposed shear rate of 10^{-4}, computed at a strain of 1.0. The PA state is shown in the extreme left and the WA state on the extreme right. In between, the states with local swap annealing are displayed, with the width of the annealing region (w) increasing from left to right, as labeled.

To summarize, this part of the study demonstrates that for states having structural heterogeneity, the shear response has a spatial profile which is determined by the properties of the undeformed state. Below, we perform a similar analysis for the second sample preparation protocol.

2. Protocol 2

As done for protocol 1, we construct the mobility maps for the five cases, corresponding to protocol 2, at a particular strain, viz., $\gamma = 1.0$; see Fig. 8. Consistent with our discussions above, we find the following: the WA state, which is the most stable glass, exhibits a very well-defined shear band (consistent with previous studies [11]); the location of the shear band, in principle, could be anywhere along z. For the PA state, the system is nearly fluidized across the system, as expected. For the cases of locally swap-annealed states,

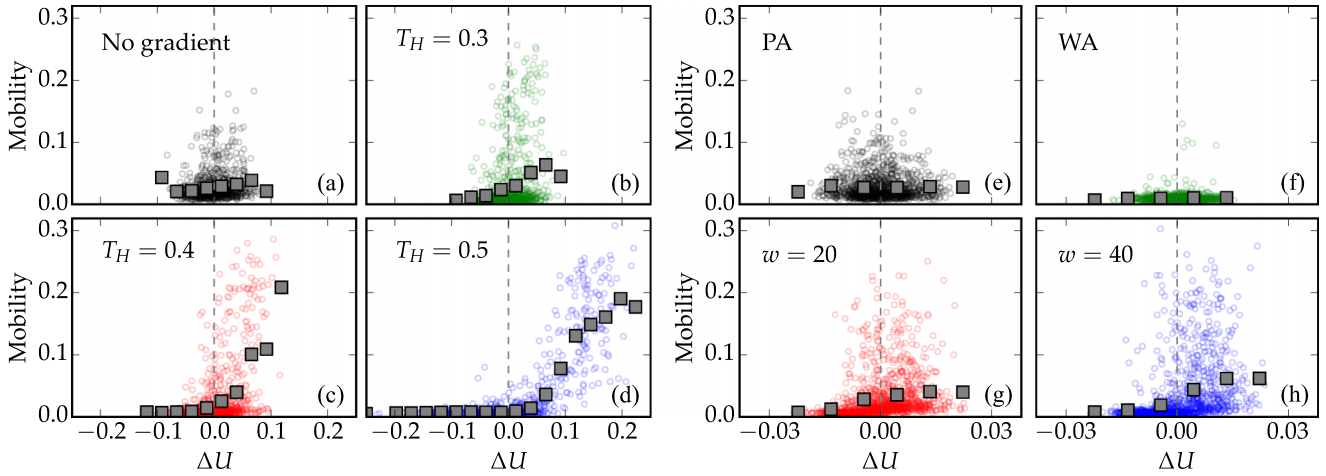

FIG. 9. Dependence of local mobility on fluctuations in local potential energy. At strain of $\gamma = 0.1$, variation of local mobility, quantified via the squared displacement (relative to the initial undeformed state), with the local fluctuations in potential energy in the initial undeformed state (i.e., at $\gamma = 0$). The scatter from individual runs (faint circles) as well as the mean behavior (filled squares) is shown for both protocol 1 [(a)–(d)] and protocol 2 [(e)–(h)].

shear banding is also observed, with the shear band being located in the region where the local energy was higher in the undeformed state, i.e., relatively less stable. Further, for these states, the broadening of the shear band also depends upon the width of the local annealing region; the larger the width of the stable region, the sharper the interface of the shear band. Thus, as evidenced via this exercise, with the local variation of stability, it is possible to engineer the location of the shear band and also its spatial growth. A quantitative correlation of this aspect is explored next.

D. Quantifying correlations

To quantify the correlations between the spatial features in the initial state and the observed spatial variation in response to the subsequently imposed shear, we construct a scatter plot of local mobility that has emerged over a strain window (quantified via the squared displacement relative to the initial state, i.e., at $\gamma = 0$) versus fluctuations in local energy in the initial undeformed state.

In practice, the following steps are done. For a single phase-space MD trajectory of the sheared N-particle system, we compute the spatial profile of local mobility, $\Delta^2(z)$, using the single-particle squared displacements δr_z^2 and then averaging along x and y at a particular z. From the initial structure corresponding to this phase-space trajectory, the profile of energy fluctuations around the mean value, viz., $\Delta U(z) = U(z) - \langle U(z)\rangle$, is generated, where $\langle . \rangle$ refers to the average of the profile along z. In the case of protocol 1, for constructing the profiles, we are using a spatial discretization of $\delta z = 2.5$, and $\delta z = 2.0$ for protocol 2. These spatial profiles, viz., $\Delta^2(z)$ and $\Delta U(z)$, are then used to construct the scatter plot of mobility (Δ^2) versus ΔU. In the scatter plots shown in Fig. 9 for both the protocols that we have studied, we show data from individual phase-space MD trajectories (shown using circles). Also shown are the data for the variation of mean mobility (shown using filled squares) with local energy fluctuations, computed by averaging over the scatter data obtained from the ensemble of independent MD trajectories, to demonstrate the overall trend in each case.

In the case of protocol 1, data are shown for 24 independent runs, for four cases, viz., where the unsheared states have not or have been subjected to any thermal gradient, with $T_H = 0.3, 0.4, 0.5$. The observed correlations are evident. For the case $T_H = 0.5$, we clearly see that the mobility is high for large and positive values of ΔU and negligible for $\Delta U < 0$. This evidences that regions which had higher local potential energies in the initial state are locations with high mobility, and there is negligible dynamics in regions which had lower energies in the initial state. This correlation is still visible for $T_H = 0.3, 0.4$, but the spread in the scatter for $\Delta U > 0$ becomes lesser with lower T_H. For the state with no thermal processing, there are no visible clear correlations between mobility and local energy fluctuations. Or, in other words, in this case, the shear band can emerge anywhere and therefore there will be stochasticity in its location. A similar behavior is observed for the case of protocol 2, as is visible for the four cases that we show, viz., the PA state, the WA state, and the two inhomogeneously annealed states having width of $w = 20, 40$. For the PA and WA states, since the shear band location can be anywhere as discussed above, there is no visible correlation between ΔU and mobility. However, when there is a contrast in local energy by construction via the inhomogeneous annealing, larger mobility occurs at regions with higher stability, i.e., $\Delta U > 0$.

IV. CONCLUSIONS

In this study, we have investigated the shear response of spatially inhomogeneous glassy samples, with the objective of analyzing whether paths of failure can be controlled via such heterogeneities and whether the underlying mechanisms for that could be identified. Unlike a previous study [35] where the consequences of introducing soft spots into amorphous solids were probed in the athermal quasistatic limit, our studies are done at finite temperatures and finite shear rates, where

stochastic effects are usually at play, as reported earlier [33]. Therefore, our pursuit is to find the necessary conditions via which such stochasticities can be surmounted by imprinting heterogeneities into the glassy sample through some physical processes.

To demonstrate the generality of our findings, we have used two different physical protocols for generating glassy states with spatial heterogeneity. In the first case, we are motivated by thermal conditions encountered during generic glass manufacturing or due to inhomogeneous heating (e.g., see Refs. [43–48]). In the second case, we consider possible situations where the extent of local annealing can be controlled which would lead to glassy states having different local stability. Our aim is to understand whether the mechanical behavior, especially the spatial response, is influenced by the initial structural heterogeneities that are generated via such protocols. Note that these are two example protocols that we have chosen for our study; however, in general there can be other circumstances via which spatially inhomogeneous glassy states can be prepared. In both the protocols that we have utilized, we obtain systematic spatial variation in local potential energy by the tuning of the relevant control parameters, with an associated variation in local density. In terms of physical mechanisms, the two protocols work in very different ways: the Soret effect in protocol 1 leads to transport of the two species in different directions relative to the thermal gradient, while the annealing via the additional swap MC leads to better local "packing" as the system's energy gets better optimized locally. Note that while the Soret effect, in the presence of the thermal gradient, leads to local compositional change which results in the observed spatial profiles of energy, the local annealing does not. In the latter case, the efficient local annealing leads to accessing of lower energy which results in the energy profiles.

We have probed the mechanical response of these samples by imposing an external drive having fixed shear rate. The macroscopic response of the inhomogeneous states, quantified via the evolution of measured stress in the sample as a function of increasing strain, is of course altered vis-a-vis the spatially homogeneous states, with the system demonstrating softer or stiffer response depending upon relative spatial scale of regions having lower/higher potential energy. In the same manner, the timescale at which the sheared states achieve steady state also shifts, with systems having more spatial span of lower potential energy taking longer to reach steady flow. The spatial insights of the failure mechanism are thereafter obtained using mobility maps, which clearly indicates that it is possible to have a control over the location of the failure via the initial spatial heterogeneity in the glassy state. In particular, the location of shear band initiation has a one-to-one correspondence with the location where the local potential energy is higher, i.e., the region having less stability. This is evidenced via our observations for both of the model protocols that we have utilized for generating the inhomogeneous states. We have further confirmed this by a thought experiment involving the stochasticity of the thermostat vis-a-vis a single heterogeneous sample and showing that stochasticity has no role to play in the location of the shear band.

The extension of this work would be to perform studies at very low temperatures, where some interesting features are expected. Also, computer experiments can be utilized to generate more variations in spatial heterogeneity aimed at targeted design, which can then be translated to experimental situations. Further, other shear directions can be explored to understand the failure mechanism and its coupling to these heterogeneities.

ACKNOWLEDGMENTS

We thank Peter Sollich for discussions. Further, we thank the HPC facility at IMSc for providing computational resources. P.C. acknowledges support via the subproject on the Modeling of Soft Materials within the IMSc Apex project funded by the Department of Atomic Energy, India. V.V. gratefully acknowledges funding from the European Union through Horizon Europe ERC Grant No. 101043968 "Multimech".

[1] C. A. Schuh, T. C. Hufnagel, and U. Ramamurty, Acta Mater. **55**, 4067 (2007).
[2] P. K. Jaiswal, I. Procaccia, C. Rainone, and M. Singh, Phys. Rev. Lett. **116**, 085501 (2016).
[3] I. Procaccia, C. Rainone, and M. Singh, Phys. Rev. E **96**, 032907 (2017).
[4] G. Parisi, I. Procaccia, C. Rainone, and M. Singh, Proc. Natl. Acad. Sci. USA **114**, 5577 (2017).
[5] M. Ozawa, L. Berthier, G. Biroli, A. Rosso, and G. Tarjus, Proc. Natl. Acad. Sci. USA **115**, 6656 (2018).
[6] A. D. S. Parmar, S. Kumar, and S. Sastry, Phys. Rev. X **9**, 021018 (2019).
[7] M. Popović, T. W. J. de Geus, and M. Wyart, Phys. Rev. E **98**, 040901(R) (2018).
[8] H. J. Barlow, J. O. Cochran, and S. M. Fielding, Phys. Rev. Lett. **125**, 168003 (2020).
[9] J. Pollard and S. M. Fielding, Phys. Rev. Res. **4**, 043037 (2022).
[10] D. Richard, C. Rainone, and E. Lerner, J. Chem. Phys. **155**, 056101 (2021).
[11] K. Lamp, N. Küchler, and J. Horbach, J. Chem. Phys. **157**, 034501 (2022).
[12] W. Götze, *Complex Dynamics of Glass-Forming Liquids: A Mode-Coupling Theory* (Oxford University Press, Oxford, 2009).
[13] R. Besseling, L. Isa, P. Ballesta, G. Petekidis, M. E. Cates, and W. C. K. Poon, Phys. Rev. Lett. **105**, 268301 (2010).
[14] T. Divoux, D. Tamarii, C. Barentin, and S. Manneville, Phys. Rev. Lett. **104**, 208301 (2010).
[15] V. Chikkadi, G. Wegdam, D. Bonn, B. Nienhuis, and P. Schall, Phys. Rev. Lett. **107**, 198303 (2011).
[16] T. Divoux, M. A. Fardin, S. Manneville, and S. Lerouge, Annu. Rev. Fluid Mech. **48**, 81 (2016).
[17] R. Maaß and J. F. Löffler, Adv. Funct. Mater. **25**, 2353 (2015).

[18] J. Bokeloh, S. V. Divinski, G. Reglitz, and G. Wilde, Phys. Rev. Lett. **107**, 235503 (2011).
[19] I. Binkowski, G. P. Shrivastav, J. Horbach, S. V. Divinski, and G. Wilde, Acta Mater. **109**, 330 (2016).
[20] R. Hubek, S. Hilke, F. A. Davani, M. Golkia, G. P. Shrivastav, S. V. Divinski, H. Rösner, J. Horbach, and G. Wilde, Front. Mater. **7**, 144 (2020).
[21] F. Varnik, L. Bocquet, J.-L. Barrat, and L. Berthier, Phys. Rev. Lett. **90**, 095702 (2003).
[22] N. P. Bailey, J. Schiotz, and K. W. Jacobsen, Phys. Rev. B **73**, 064108 (2006).
[23] Y. Shi and M. L. Falk, Phys. Rev. B **73**, 214201 (2006).
[24] Y. Shi, M. B. Katz, H. Li, and M. L. Falk, Phys. Rev. Lett. **98**, 185505 (2007).
[25] Y. Ritter and K. Albe, Acta Mater. **59**, 7082 (2011).
[26] D. Şopu, Y. Ritter, H. Gleiter, and K. Albe, Phys. Rev. B **83**, 100202(R) (2011).
[27] P. Chaudhuri, L. Berthier, and L. Bocquet, Phys. Rev. E **85**, 021503 (2012).
[28] R. Dasgupta, H. G. E. Hentschel, and I. Procaccia, Phys. Rev. Lett. **109**, 255502 (2012).
[29] R. Dasgupta, O. Gendelman, P. Mishra, I. Procaccia, and C. A. B. Z. Shor, Phys. Rev. E **88**, 032401 (2013).
[30] K. Albe, Y. Ritter, and D. Sopu, Mech. Mater. **67**, 94 (2013).
[31] O. Gendelman, P. K. Jaiswal, I. Procaccia, B. Sen Gupta, and J. Zylberg, Europhys. Lett. **109**, 16002 (2015).
[32] G. P. Shrivastav, P. Chaudhuri, and J. Horbach, Phys. Rev. E **94**, 042605 (2016).
[33] M. Golkia, G. P. Shrivastav, P. Chaudhuri, and J. Horbach, Phys. Rev. E **102**, 023002 (2020).
[34] M. Singh, M. Ozawa, and L. Berthier, Phys. Rev. Mater. **4**, 025603 (2020).
[35] M. Ozawa, L. Berthier, G. Biroli, and G. Tarjus, Phys. Rev. Res. **4**, 023227 (2022).
[36] Z. Fan, E. Ma, and M. L. Falk, Phys. Rev. Mater. **6**, 065602 (2022).
[37] W. Kob and H. C. Andersen, Phys. Rev. E **51**, 4626 (1995).
[38] V. Vaibhav, J. Horbach, and P. Chaudhuri, Phys. Rev. E **101**, 022605 (2020).
[39] A. Ninarello, L. Berthier, and D. Coslovich, Phys. Rev. X **7**, 021039 (2017).
[40] N. Küchler and J. Horbach, Phys. Rev. E **106**, 064103 (2022).
[41] N. Küchler and J. Horbach, Phys. Rev. E **108**, 024127 (2023).
[42] T. S. Grigera and G. Parisi, Phys. Rev. E **63**, 045102(R) (2001).
[43] M. K. Choudhary, R. Venuturumilli, and M. R. Hyre, Int. J. Appl. Glass Sci. **1**, 188 (2010).
[44] D. Clever and J. Lang, Optim. Control Appl. Meth. **33**, 157 (2012).
[45] C. A. Angell, Solid State Ion. **18-19**, 72 (1986).
[46] Y. Liu, C. T. Liu, E. P. George, and X. Z. Wang, Appl. Phys. Lett. **89**, 051919 (2006).
[47] M. D. Ediger, J. Chem. Phys. **147**, 210901 (2017).
[48] Y. Liu, M. Shimizu, B. Zhu, Y. Dai, B. Qian, J. Qiu, Y. Shimotsuma, K. Miura, and K. Hirao, Opt. Lett. **36**, 2161 (2011).
[49] S. Plimpton, J. Comput. Phys. **117**, 1 (1995).
[50] M. Ozawa, L. Berthier, G. Biroli, and G. Tarjus, Phys. Rev. Res. **2**, 023203 (2020).
[51] T. Soddemann, B. Dünweg, and K. Kremer, Phys. Rev. E **68**, 046702 (2003).